Black hole and accretion disk formation in the collapsar model

Yuichiro Sekiguchi[1][(a),(b)],

[(a)] *Yukawa Institute, Kyoto University, Kyoto 606-8502*
[(b)] *Division of Theoretical Astronomy, National Astronomical Observatory of Japan, Tokyo 181-8588*

Abstract

Recent studies of modeling a progenitor of long gamma-ray bursts (LGRBs) suggest that progenitors of LGRBs might have a core with higher entropy than that of ordinary presupernove. Based on the above suggestion, we performed fully general relativistic, two-dimensional simulations of collapse of *higher entropy* core to a black hole. As for the microphysics, we took into account a realistic EOS, weak interaction processes such as electron capture and pair-neutrino processes, and neutrino cooling by a recently develpoed general relativistic leakage scheme. The initial core is simply modeled by a equilibrium configuration with constant entropy and electron fraction. We found that (1) the core experiences gas pressure dominated bounce before it collapses to a black hole as in previsou simulations. (2) After the black hole formation, a thin accretion disk is formed. (3) Shock waves are formed at the inner part of the disk as infalling matters strike the disk. (4) The thin disk expands to be a thick torus accumulating the thermal energy generated at the shocks. (4) Convection occurs inside the torus because of the formation of negative entropy gradient. (5) As a result, neutrino luminosity shows violent time variability. We clarify the mechanism of these results. We also discuss importance of black hole spin on the dynamics and properties of the accretion flows around the black hole.

1   Introduction

Gamma-ray bursts (GRBs) have been one of the outstanding problems in astrophysics since their discovery. The large amount of energy release, short duration, and variability timescale indicates that GRBs may be associated with accretion processes onto a stellar-mass size black hole [1].

Although progenitors of GRBs have not been fully clarified yet, there is accumulating observational evidence that LGRBs are associated with collapse of massive stars [2]. Recent observations indicate that LGRBs may prefer a low metallicity environment [3, 4]. Therefore, gravitational collapse of population III (Pop III) stars, which are formed out of metal-free gas, may be accompanied by LGRB at a very high redshift [5]. On the other hand, it is recently showed that a single star can fulfill the requirements of the collapsar models if it is initially rapidly rotating ($\gtrsim 50\%$ of the Keplerian velocity at the equatorial surface) and of low metallicity ($Z/Z_\odot \lesssim 0.1$) [7?].

There have been other progenitor models of LGRBs (for a recent review, see[8]). Some authors [9] proposed binary-interaction models, in which the tidal force in a close binary keeps a helium star in synchronous, rapid rotation. It is also sugested that [10] a helium star in a close binary with a compact companion (i.e., neutron star or black hole) can retain sufficient angular momentum to form a progenitor of a GRB. Fryer and Heger [11] suggested a binary-merger model and showed that a merger of two helium cores during the common-envelope inspiral phase can produce a rapidly rotating core which satisfies the requirement of the collapsar models.

All of them are anomalous in the sense that they are quite different from the progenitors of ordinary supernovae. Qualitatively speaking, the progenitor models have larger angular momentum and *higher entropy* (and hence, more massive). The chemically homogeneous models predict a well-mixed, larger core with higher central entropy than the ordinary supernova core. It is also expected that the object formed after the binary merger will have a higher entropy, if the mass ratio of merging stars is not far from unity [12].

---

[1]Email address: sekig@yukawa.kyoto-u.ac.jp

Such a massive stellar core may collapse directly to a black hole without producing any explosion (Type III collapsar) [13]. In this article, we perform fully general relativistic simulations of collapse of rapidly rotating, higher entropy core in the context of the Type III collapsar, taking into account detailed microphysics, that is, a realistic equation of state (EOS), weak interaction processes such as electron capture and pair-neutrino processes, and neutrino cooling.

2 Setting

2.1 Hydrodynamic equations in general relativistic leakage scheme

Recently, I developed a fully general relativistic hydrodynamic code implementing a realistic equation of state, self-consistent electron and positron captures, and neutrino cooling by a general relativistic leakage scheme [14]. We follow this paper in solving hydrodynamic equations for which the readers may refer to the details. We assume the axial and equatorial symmetry of the spacetime and the hydrodynamics equations are solved in the cylindrical coordinates (ϖ, φ, z) where $\varpi = \sqrt{x^2 + y^2}$.

2.1.1 Energy-momentum conservation equation

The basic equations of general relativistic hydrodynamics with neutrinos are

$$\nabla_\alpha (T^{\mathrm{Total}})^\alpha_\beta = \nabla_\alpha \left[(T^{\mathrm{F}})^\alpha_\beta + (T^\nu)^\alpha_\beta \right] = 0, \tag{1}$$

where $(T^{\mathrm{Total}})_{\alpha\beta}$ is the total energy-momentum tensor, and $(T^{\mathrm{F}})_{\alpha\beta}$ and $(T^\nu)_{\alpha\beta}$ are the energy-momentum tensor of fluids and neutrinos, respectively. The neutrino energy-momentum tensor is decomposed into 'trapped-neutrino' $((T^{\nu,\mathrm{T}})_{\alpha\beta})$ and 'streaming-neutrino' $((T^{\nu,\mathrm{S}})_{\alpha\beta})$ parts as

$$(T^\nu)_{\alpha\beta} = (T^{\nu,\mathrm{T}})_{\alpha\beta} + (T^{\nu,\mathrm{S}})_{\alpha\beta}. \tag{2}$$

Here, the trapped-neutrinos phenomenologically represent neutrinos which interact sufficiently frequently with matter and are thermalized, and the streaming-neutrino part describes a phenomenological flow of neutrinos streaming out of the system.

The streaming-neutrinos are produced with a leakage rate Q_α^{leak} according to

$$\nabla_\beta (T^{\nu,\mathrm{S}})^\beta_\alpha = Q_\alpha^{\mathrm{leak}}. \tag{3}$$

On the other hand, the trapped-neutrino part is combined with the fluid part as

$$T_{\alpha\beta} \equiv (T^{\mathrm{F}})_{\alpha\beta} + (T^{\nu,\mathrm{T}})_{\alpha\beta}. \tag{4}$$

Then the equation for $T_{\alpha\beta}$ is

$$\nabla_\beta T^\beta_\alpha = -Q_\alpha^{\mathrm{leak}}. \tag{5}$$

We solve Eqs (3) and (5) for the energy-momentum conservation equation.

The energy-momentum tensor of the fluid and trapped-neutrino parts $(T_{\alpha\beta})$ is treated as that of the perfect fluid,

$$T_{\alpha\beta} = (\rho + \rho\varepsilon + P)u_\alpha u_\beta + P g_{\alpha\beta}, \tag{6}$$

where ρ and u^α are the rest mass density and the 4-velocity. The specific internal energy density (ε) and the pressure (P) are the sum of contributions from the baryons (free protons, free neutrons, α-particles, and heavy nuclei), leptons (electrons, positrons, and *trapped-neutrinos*), and the photons.

The streaming-neutrino part, on the other hand, is set to be a general form of

$$(T^{\nu,\mathrm{S}})_{\alpha\beta} = E n_\alpha n_\beta + F_\alpha n_\beta + F_\beta n_\alpha + P_{\alpha\beta}, \tag{7}$$

where $F_\alpha n^\alpha = P_{\alpha\beta} n^\alpha = 0$. In order to close the system, we need an explicit expression of $P_{\alpha\beta}$. In this paper, we adopt a simple form $P_{\alpha\beta} = \chi E \gamma_{\alpha\beta}$ with $\chi = 1/3$. This approximation may work well in high density regions but will violate in low density regions. However, the violation will not affect the dynamics because the total amount of streaming-neutrinos emitted in low density regions will be small.

2.1.2   Lepton-number conservation equations

The conservation equations of the lepton fractions are written schematically as

$$\frac{dY_e}{dt} = -\gamma_e, \tag{8}$$

$$\frac{dY_{\nu_e}}{dt} = \gamma_{\nu_e}, \quad \frac{dY_{\bar{\nu}_e}}{dt} = \gamma_{\bar{\nu}_e}, \tag{9}$$

$$\frac{dY_{\nu_x}}{dt} = \gamma_{\nu_x}, \tag{10}$$

where Y_e, Y_{ν_e}, $Y_{\bar{\nu}_e}$, and Y_{ν_x} denote the electron fraction, the electron neutrino fraction, the electron anti-neutrino fraction, and μ and τ neutrino and anti-neutrino fractions, respectively. The source terms are given by $\gamma_e = \gamma_{\nu_e}^{\rm local} - \gamma_{\bar{\nu}_e}^{\rm local}$, $\gamma_{\nu_e} = \gamma_{\nu_e}^{\rm local} - \gamma_{\nu_e}^{\rm leak}$, $\gamma_{\bar{\nu}_e} = \gamma_{\bar{\nu}_e}^{\rm local} - \gamma_{\bar{\nu}_e}^{\rm leak}$, and $\gamma_{\nu_x} = \gamma_{\nu_x}^{\rm local} - \gamma_{\nu_x}^{\rm leak}$, where $\gamma^{\rm local}$'s and $\gamma^{\rm leak}$'s are the local production and leakage rates of each neutrino, respectively. Because $\gamma_\nu^{\rm local}$'s are characterized by the timescale of weak-interaction processes $t_{\rm wp} \sim |Y_e/\dot{Y}_e|$ which can be much shorter than the dynamical timescale, the direct and explicit solution of Eqs (8)–(10) will be unstable. Therefore we follow the procedure proposed in [14] to solve the equations stably in an explicit manner.

First, in each timestep n, the conservation equation of the *total* lepton fraction ($Y_l = Y_e - Y_{\nu_e} + Y_{\bar{\nu}_e}$),

$$\frac{dY_l}{dt} = -\gamma_l, \tag{11}$$

is solved together with the conservation equation of Y_{ν_x}, Eq. (10), in advance of solving whole of the lepton conservation equations (Eqs. (8) – (10)). Then, assuming that the β-equilibrium is achieved, values of the lepton fractions in the β-equilibrium (Y_e^β, $Y_{\nu_e}^\beta$, and $Y_{\bar{\nu}_e}^\beta$) are calculated from the evolved Y_l.

Second, regarding $Y_{\nu_e}^\beta$ and $Y_{\bar{\nu}_e}^\beta$ as the maximum allowed values of the neutrino fractions in the next timestep $n+1$, the source terms are limited so that Y_ν's in the timestep $n+1$ cannot exceed Y_ν^β 's. Then, the whole of the lepton conservation equations (Eqs. (8) – (10)) are solved explicitly using these limiters.

Third, the conditions $\mu_p + \mu_e < \mu_n + \mu_{\nu_e}$ and $\mu_n - \mu_e < \mu_p + \mu_{\bar{\nu}e}$ are checked, where μ_p, μ_n, μ_e, μ_{ν_e} and $\mu_{\bar{\nu}e}$ are the chemical potentials of protons, neutrons, electrons, electron neutrinos, and electron anti-neutrinos, respectively. If both conditions are satisfied, the values of the lepton fractions in the timestep $n+1$ are set to be those in the β-equilibrium value; Y_e^β, $Y_{\nu_e}^\beta$, and $Y_{\bar{\nu}_e}^\beta$. On the other hand, if either or both conditions are not satisfied, the lepton fractions in the timestep $n+1$ is set to be those obtained by solving whole of the lepton-number conservation equations.

2.2   Microphysics

2.2.1   Equation of state

In this paper, we employ an EOS by Shen et al [15], which is derived by the relativistic mean field theory based on the relativistic Brückner-Hartree-Fock theory. The thermodynamical quantities of dense matter at various sets of (ρ, Y_p, T) are calculated to construct the numerical data table for simulation. The table covers a wide range of density $10^{5.1}$–$10^{15.4}$ g/cm^3, electron fraction 0.0–0.56, and temperature 0–100 MeV, which are required for supernova simulation.

To consistently calculate the pressure and the internal energy of the electron and positron, the charge neutrality condition $Y_p = Y_e$ should be solved to determine the electron chemical potential μ_e for each value of the baryon rest-mass density ρ and the temperature T in the EOS table. Then, assuming that the electrons and positrons obey the Fermi-Dirac distribution, the number density, the pressure, and the internal energy density of electrons and positrons are calculated.

The pressure and the specific internal energy density of photons are given by $P_r = a_r T^4/3$ and $\varepsilon_r = a_r T^4/\rho$, where a_r is the radiation constant $a_r = (\pi^2 k_B^4)/(15 c^3 \hbar^3)$ and c is the velocity of light.

In this paper, the trapped-neutrinos are assumed to interact sufficiently frequently with matter that be thermalized. Therefore they are described as ideal Fermi gases with the matter temperature. Then, from the neutrino fractions Y_ν, the chemical potentials of neutrinos are calculated by solving $Y_\nu = Y_\nu(\mu_\nu, T)$. Using the chemical potentials, μ_ν, and the matter temperature, the pressure and the internal energy of the trapped-neutrinos are calculated in the same manner as for electrons.

2.2.2   Weak interaction and leakage rate

The leakage rates are defined by [14]

$$Q_\nu^{\text{leak}} = (1 - e^{-b\tau_\nu})Q_\nu^{\text{diff}} + e^{-b\tau_\nu}Q_\nu^{\text{local}}, \tag{12}$$

$$\gamma_\nu^{\text{leak}} = (1 - e^{-b\tau_\nu})\gamma_\nu^{\text{diff}} + e^{-b\tau_\nu}\gamma_\nu^{\text{local}}, \tag{13}$$

where τ_ν is the optical depth of neutrinos and b is a parameter which is typically set as $b^{-1} = 2/3$. Then, because Q_ν^{leak} may be regarded as the emissivity of neutrinos measured in the *fluid rest frame*, Q_α^{leak} is defined as

$$Q_\alpha^{\text{leak}} = Q_\nu^{\text{leak}} u_\alpha. \tag{14}$$

As the local production reactions of neutrinos, the electron and positron captures ($\gamma_{\nu_e}^{\text{ec}}$ and $\gamma_{\bar{\nu}_e}^{\text{pc}}$), the electron-positron pair annihilation ($\gamma_{\nu_e\bar{\nu}_e}^{\text{pair}}$ for electron-type neutrinos and $\gamma_{\nu_x\bar{\nu}_x}^{\text{pair}}$ for the other type), the plasmon decays ($\gamma_{\nu_e\bar{\nu}_e}^{\text{plas}}$ and $\gamma_{\nu_x\bar{\nu}_x}^{\text{plas}}$), and the Bremsstrahlung processes ($\gamma_{\nu_e\bar{\nu}_e}^{\text{Brems}}$ and $\gamma_{\nu_x\bar{\nu}_x}^{\text{Brems}}$), are considered in this paper. Then, the local rates for the neutrino fractions are

$$\gamma_{\nu_e}^{\text{local}} = \gamma_{\nu_e}^{\text{ec}} + \gamma_{\nu_e\bar{\nu}_e}^{\text{pair}} + \gamma_{\nu_e\bar{\nu}_e}^{\text{plas}} + \gamma_{\nu_e\bar{\nu}_e}^{\text{Brems}}, \tag{15}$$

$$\gamma_{\bar{\nu}_e}^{\text{local}} = \gamma_{\bar{\nu}_e}^{\text{pc}} + \gamma_{\nu_e\bar{\nu}_e}^{\text{pair}} + \gamma_{\nu_e\bar{\nu}_e}^{\text{plas}} + \gamma_{\nu_e\bar{\nu}_e}^{\text{Brems}}, \tag{16}$$

$$\gamma_{\nu_x}^{\text{local}} = \gamma_{\nu_x\bar{\nu}_x}^{\text{pair}} + \gamma_{\nu_x\bar{\nu}_x}^{\text{plas}} + \gamma_{\nu_x\bar{\nu}_x}^{\text{Brems}}. \tag{17}$$

Similarly, the local neutrino energy emission rate Q_ν^{local} is given by

$$
\begin{aligned}
Q_\nu^{\text{local}} = Q_{\nu_e}^{\text{ec}} + Q_{\bar{\nu}_e}^{\text{pc}} \quad &+ \quad 2\,(Q_{\nu_e\bar{\nu}_e}^{\text{pair}} + Q_{\nu_e\bar{\nu}_e}^{\text{plas}} + Q_{\nu_e\bar{\nu}_e}^{\text{Brems}}) \\
&+ \quad 4\,(Q_{\nu_x\bar{\nu}_x}^{\text{pair}} + Q_{\nu_x\bar{\nu}_x}^{\text{plas}} + Q_{\nu_x\bar{\nu}_x}^{\text{Brems}})\,.
\end{aligned}
\tag{18}
$$

The explicit forms of the local rates in Eqs. (15)–(18) will be found in [14].

We follow the recent work by Rosswog and Liebendörfer [16] for the diffusive neutrino emission rates γ_ν^{diff} and Q_ν^{diff} in Eqs (12) and (13). The explicit forms of γ_ν^{diff} and Q_ν^{diff} will be found in [14].

2.3   Initial condition and Grid

We construct approximate initial models in the following manner. We first calculate a spherical equilibrium configuration with a constant electron fraction of $Y_e = 0.5$ and with a constant entropy per baryon $s = 8k_B$. We set the central density to be $\rho_c \approx 10^8$ g/cm^3. The corresponding central temperature is $T_c \approx 9 \times 10^9$ K. Following Nakazato et al. [17], we define the boundary of the iron core to be where the temperature is 5×10^9 K. Then the mass and the radius of the iron core are $M_{\text{iron}} \approx 13 M_\odot$ and $R_{\text{iron}} \approx 7000$ km. We adopt a wider region of $R_{\text{init}} \approx 14000$ km with mass of $M_{\text{init}} \approx 23 M_\odot$.

At the current status, little is known about the angular momentum distribution in the progenitor core. Therefore we add the following rotation profile model

$$\Omega(\varpi) = \Omega_0 \exp\left[-\frac{1}{2}\frac{R_c^2}{(\varpi^2 + R_c^2)}\right] \exp\left[-\frac{\varpi^2}{R_0^2}\right], \tag{19}$$

where Ω, R_0 and R_c are parameters which control the degree of differential rotation. We fix the values of R_0 and R_c as $R_0 = R_{\text{init}}/5$ and $R_c = R_{\text{init}}/8$ and vary Ω_0 as 0, 0.4, 0.5 and 0.6 (hereafter referred to

	$\Phi_c \leq 0.0125$	$\leq \Phi_c \leq 0.025$	$\leq \Phi_c \leq 0.05$	$\leq \Phi_c \leq 0.1$	$\Phi_c \leq 0.2$	$\Phi_c \geq 0.2$
Δx_0	10.1	4.8	2.2	0.98	0.45	0.22
δ	0.008	0.0075	0.007	0.0065	0.006	0.0065
N	316	412	524	652	796	960
L (km)	14600	13300	11800	10100	8700	7700

Table 1: Summary of the regridding procedure. The values of the minimum grid spacing Δx_0 (in units of km), the non-uniform-grid factor δ, and the grid number N for each range of $\Phi_c = 1 - \alpha_c$ are listed.
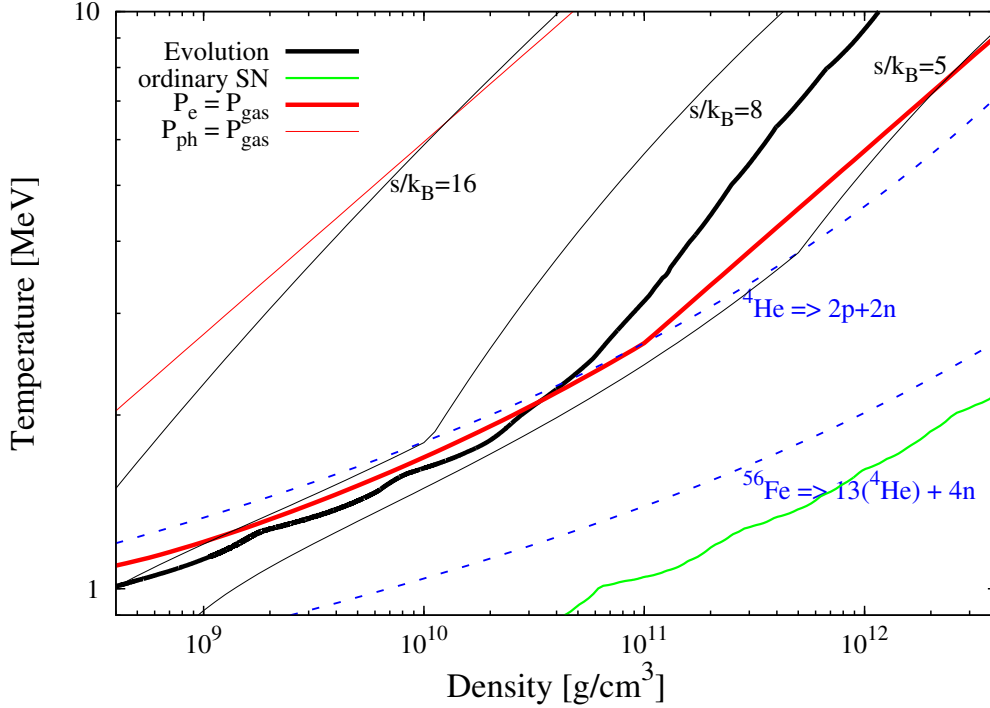
Figure 1: Evolution path of the central values of density and temperature for the spherical model in ρ-T plane (thick black solid curve). The thick and thin red solid curves show the boundary at which the condition $P_e = P_{\text{gas}}$ or $P_r = P_{\text{gas}}$ is satisfied. The thin black solid curves show evolution paths with constant entropy per baryon for $s/k_B = 5$, 8 and 16. The two blue dashed curves denote the value of (ρ, T) with which ^{56}Fe or ^{4}He will be half by mass due to the photo-dissociation. An evolution path of the central values of density and temperature for a usual supernova core is shown together (solid green curve).

as spherical, slowly rotating, moderately rotating, and rapidly rotating models). It should be addressed that the initial models adopted in this paper are *slowly rotating* in the sense the rotation imposed is much smallar than that considered in previous studies.

In numerical simulations, we adopt a nonuniform grid, in which the grid spacing is increased as $dx_{j+1} = (1 + \delta)dx_j$, $dz_{l+1} = (1 + \delta)dz_l$, where $dx_j \equiv x_{j+1} - x_j$, $dz_l \equiv z_{l+1} - z_l$, and δ is a constant. In addition, a regridding technique [18] is adopted to assign a sufficiently large number of grid points inside the collapsing core, saving the CPU time efficiently (see Table 1).

3   Results

As in the collapse of an ordinary supernova core for which the central value of entropy per baryon is $s/k_B \sim 1$, gravitational collapse is triggered by the electron capture and the photo-dissociation of heavy nuclei. In the present case, the photo-dissociation is more important for destabilizing the core because of the higher value of the entropy per baryon ($s/k_B = 8$). Due to the photo-dissociation, most of irons are resolved into heliums. As the collapse proceeds, heliums are resulved into free nucleons (p, n).

3.1   Gas pressure dominated bounce

It is known that an ordinary supernova core experiences a bounce when the central density exceeds the nuclear density ($\rho_{\text{nuc}} \sim 2 \times 10^{14}$ g/cm^3) where the pressure increases drastically due to the repulsive nuclear force. In the present case, by contrast, the collapse is not decelerated by the nuclear force but by
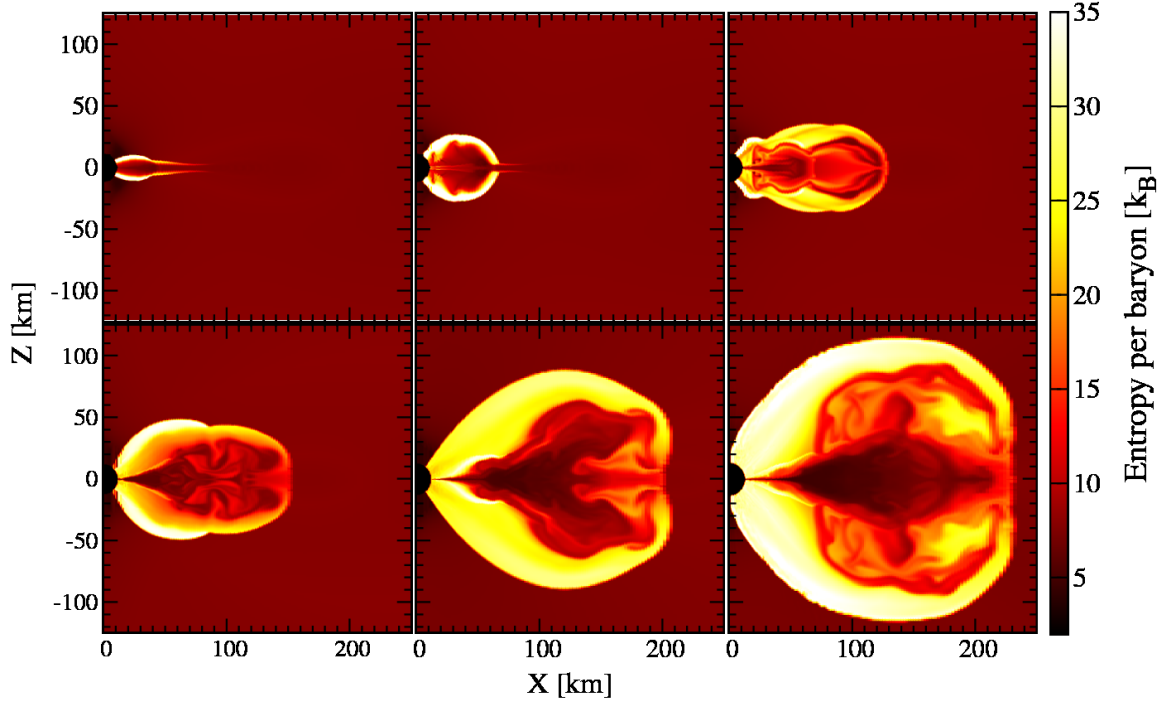
Figure 2: Contours of entropy per baryon at $t \approx 1578$ (top left), 1584 (top middle), 1591 (top right), 1644 (bottom left), 1706 (bottom middle) and 1800 ms (bottom right) for the moderately rotating model.

the thermal gas pressure P_{gas} [17]. Because the adiabatic index of non-relativistic gas is $\Gamma = 5/3$, which is much larger than that for the degenerate pressure of electrons (P_e), for which $\Gamma \approx 4/3$, the collapse is halted. The central density at bounce is below the nuclear density ($\approx 2 \times 10^{12}$ g/cm^3) and the central value of the temperature is ≈ 13 MeV.

The thick red curve in Figure 1 indicates the boundary in the ρ-T plane where the condition $P_e = P_{\mathrm{gas}}$ is satisfied ($P_e > P_{\mathrm{gas}}$ in the right-side of this curve). Evolution path of the central density and temperature in the ρ-T plane (the thick black curve in Figure 1) crosses the condition $P_e = P_{\mathrm{gas}}$, and hence, the pressure is dominated by the thermal gas pressure for $\rho \gtrsim 3 \times 10^{10}$ g/cm^3. Note that the pressure of the photon (P_{ph}) is much smaller than the gas pressure in the density and temperature region considered here; the thin red curve in Figure 1 shows where the condition $P_{\mathrm{ph}} = P_{\mathrm{gas}}$ is satisfied.

It is also clear from Figure 1 that ordinary supernova cores do not experience the thermal-pressure dominated bounce. We plot an evolution path of collapse of an supernova core , simulated in [14], in Figure 1 (see the green curve).

3.2   Black hole and thin accretion disk formation

In the moderately rotating model, the apparent horizon is first formed at $t \approx 1373$ ms with mass of $\approx 6.5 M_\odot$ and spin paramter of ≈ 0.6. Soon after the apparent horizon is formed, a thin accretion disk is formed around the black hole.

At the same time, shocks are formed at the inner part of the disk, converting the kinetic energy of the infall into the thermal energy. However, the thermal energy is immediately carried away by neutrinos because the cooling timescale of neutrino emission, t_{cool}, is very small due to the low density and small pressure scale height of the disk, H. Here, the neutrino-cooling timescale is given by $t_{\mathrm{cool}} \sim H\tau_\nu/c$.

The pressure scale height may be approximately determined by the following balance relation

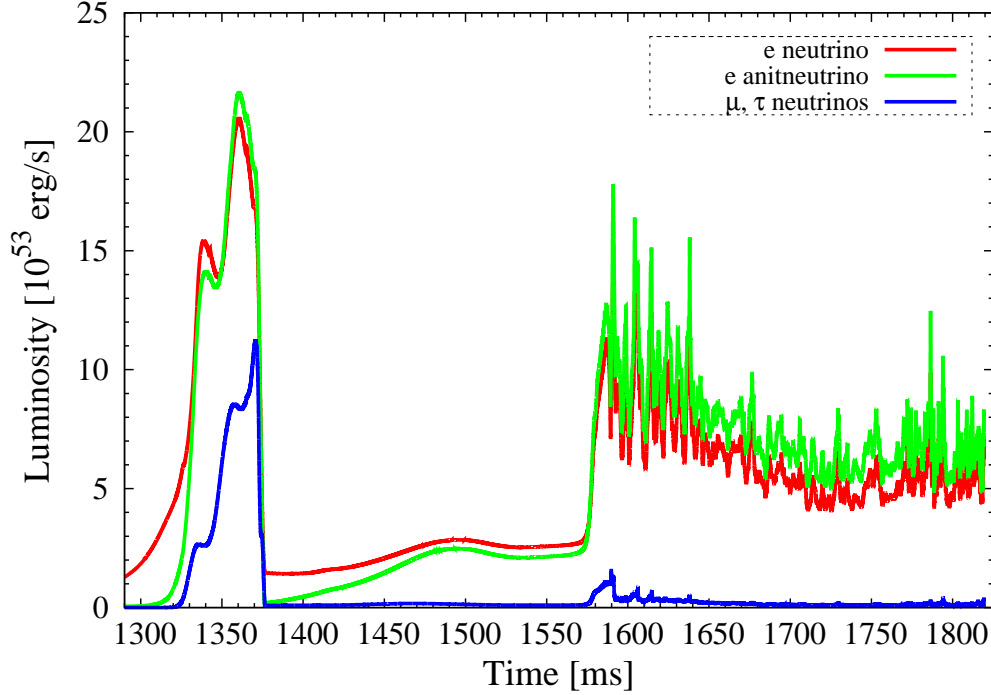$$\frac{P_{\mathrm{disk}} - P_{\mathrm{ram}}}{H} \sim \frac{GM_{\mathrm{BH}}\rho_s H}{R_{\mathrm{disk}}^3}, \tag{20}$$

Figure 3: Time evolution of neutrino luminosities for moderately rotating model.

where $R_{\mathrm{disk}}(\approx r_{\mathrm{ISCO}})$, ρ_{disk}, and P_{disk} are characteristic radius, density, and pressure of the disk, and P_{ram} is the ram pressure of the infalling matter, respectively. Equation (20) gives

$$\frac{H}{R_{\mathrm{disk}}} \sim \left(\frac{P_{\mathrm{disk}} - P_{\mathrm{ram}}}{10^{30} \text{ dyn/cm}^2} \right)^{1/2} \left(\frac{\rho_{\mathrm{disk}}}{10^{10} \text{ g/cm}^3} \right)^{1/2}. \tag{21}$$

Because the density and temperature are low due to the rapid advection and the copious neutrino emission, $P_{\mathrm{disk}} - P_{\mathrm{ram}}$ is very small, and hence, $H/R_{\mathrm{disk}} \ll 1$.

3.3   Disk expansion and torus formation

As matters with higher specific angular momentum in the outer region fall onto the disk, t_{cool} increases because neutrino optical depth and the pressure scale height increase. When density and pressure scale height become sufficiently large, the neutrino-cooling timescale becomes longer than the advection timescale onto black hole, and consequently, neutrinos are *trapped* in the accretion flow. The accretion timescale decreases because the angular momentum of the disk increases. Then, thermal energy generated by the shock heating begins to be stored efficiently and the internal energy of the disk increases (see the top-left panel in Figure 2).

As the thermal energy is stored, the disk height H increases according to Eq. (20). The density and the temperature (T_{disk}) inside the disk eventually increase to be $\sim 10^{11}$ g/cm^3 and $\sim 5 \times 10^{11}$ K (and hence, $P_{\mathrm{disk}} \sim 10^{30}$ dyn/cm^2). At the same time, the ram pressure decreases to be $\lesssim 0.1 P_{\mathrm{disk}}$ ($\ll P_{\mathrm{disk}}$) because the density of the infalling matter decreases to $\lesssim 10^9$ g/cm^3. Consequently, H increases to be $\sim R_{\mathrm{disk}}$ (see the top-middle panel in Figure 2). Then, the approximate balance relation (20) changes to

$$(P_{\mathrm{disk}} - P_{\mathrm{ram}}) \sim \frac{GM_{\mathrm{BH}}\rho_{\mathrm{disk}}}{H}. \tag{22}$$

Because the binding due to the gravitational force by the black hole decreases as H increases, the disk expands forming shock waves.
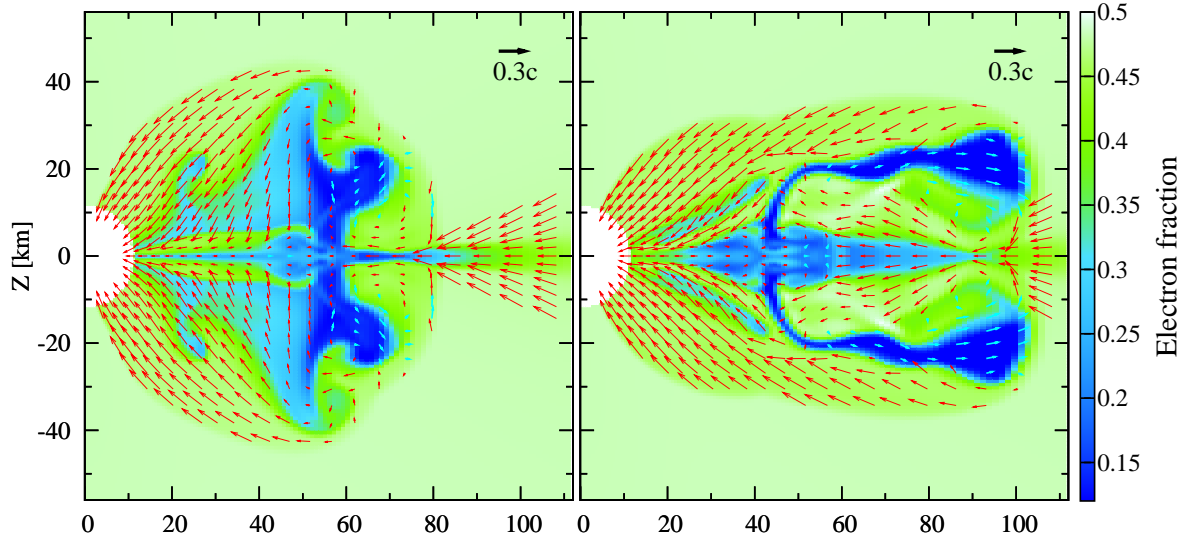
Figure 4: Contours of electron fraction with velocity fields at $t \approx 1589$ (left panel) and 1590 (right panel).

The neutrino opacities decrease as the disk expands (density and temperature decreases), and accordingly, the shock wave is stalled and the disk relaxes to a new geometrically thick state. Subsequently, the shock becomes standing accretion shock and expands gradually because matters with higher specific angular momentum falls onto the shock and because the ram pressure of the infall matters continues to decrease (see the bottom panels in Figure 2).

3.4   Convective activities

After the formation of the geometrically thick torus, convective motions are excited in the torus and the shocked region. The shock heating will be more efficient at the inner part of the disk because the kinetic energy of infall matters is larger (see the top-left panel in Figure 2). On the other hand, the neutrino cooling will be less efficient at the inner part of the disk because the disk is more optically thick to neutrinos. Then, the entropy per baryon becomes higher in the inner part of the disk and consequently, regions of negative entropy gradient are formed. Also, because neutrinos are trapped and β-equilibrium is achieved at the inner part of the disk, the total lepton fraction increases inward. These tendencies are enhanced as the accretion of matters with higher angular momentum proceeds.

Such configurations are known to be unstable to convection: The condition for convective instability to occur is given by the so-called Solberg-Hoiland criterion

$$N_{\mathrm{SH}}^2 = N_{\mathrm{BV}}^2 + \kappa^2 < 0, \tag{23}$$

where N_{BV} is the Brunt-Väisälä frequency and κ is the epicyclic frequency.

Figure 4 plots contours of electron fraction with velocity fields of matters. The convective flows cannot proceed freely because there is accretion flows outside the torus. Interacting with the thin accretion flows, a part of the convective flows is swerved to form finger-like structure (see the top-right panel in Figure 4). Note that there is velocity shear at the interface between the convective fingers and the accretion flows (see the right panel in Figure 4), and hence, the Kelvin-Helmholtz instability could be developed at the interface, generating turbulent motions.

Associated with the convective motions, shock waves are formed and accretion flows show very complicated features. Because of interplay of the neutrino-trapping, the Kelvin-Helmholtz instability, and the convective shock, the accretion flows remain convectively unstable. Figure 5 shows the Solberg-Hoiland
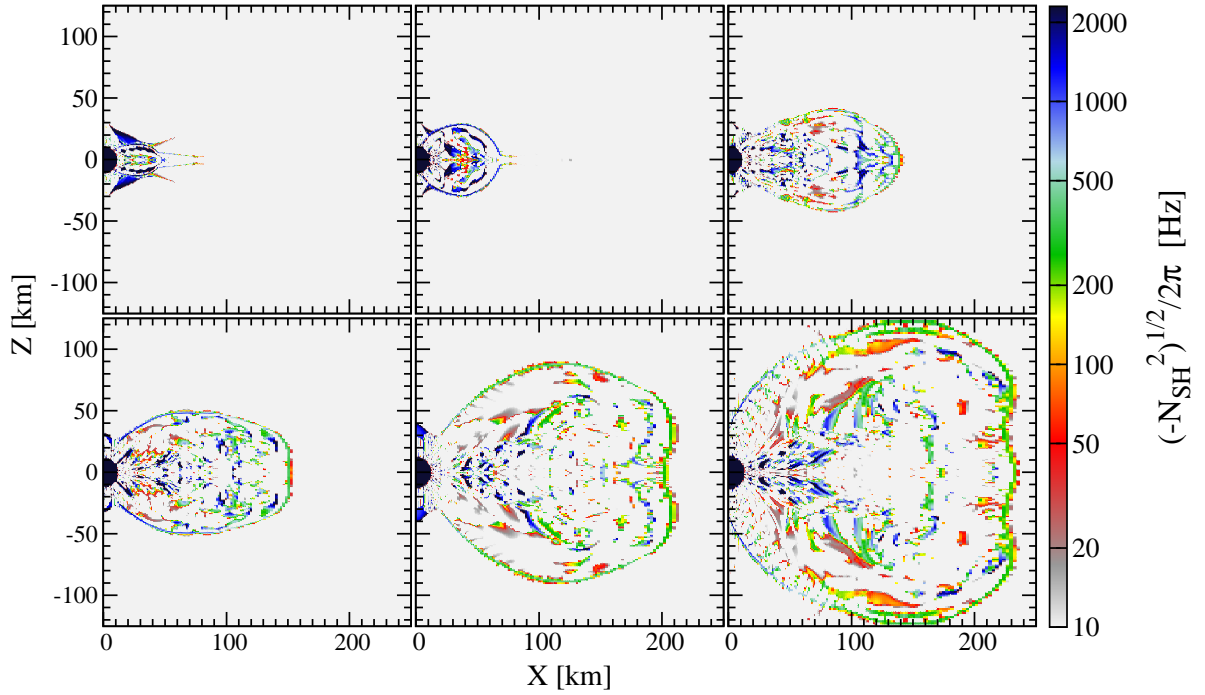
Figure 5: Contours of the frequency in Eq. (23) for the moderately rotating model. The selected timesclices are the same as those in Figure 2.

frequency, N_{SH} defined in Eq. (23). As this figure shows, the region below the shock remains convectively unstable.

As a natural consequence of the convective activities of accretion flows, neutrino luminosities vary violently in time (see Figure 3). Such time-variability may be associated with the observed time-variability of GRB light curves. Furthermore, electrons in the convective regions are only weakly degenerate due to the high entropy and temperature. Consequently, electron neutrinos and electron antineutrinos are approximately identically emitted. This is favorable for the pair annihilation of neutrinos to electron-positron pairs because its rate is proportional to $L_\nu L_{\bar\nu}$.

4   Discussions

The spin of a black hole plays crucial role on the dynamics of accretion flows. As clearly shown by [19], an accretion disk around a rapidly rotating black hole is remarkably different from that around a Schwarzschild black hole. The inner edge of the disk around a rotating black hole extends much closer to the black hole, and consequently, the temperature and density of the disk reach higher values. These have significant effects on the properties of disk against neutrinos.

Here, it should be noted that the trapping of neutrinos and occurrence of convective motions are not likely to be special consequences of the high mass accretion rate ($\dot{M} \sim 10 M_\odot$ s^{-1}) achieved in our models. According to the result by [19], the neutrino trapping occurs even with a moderate mass accretion rate of $\dot{M} \sim M_\odot$ s^{-1} for accretion flows around a rapidly rotating Kerr black hole. For accretion flows around a Schwarzschild black hole, by contrast, the neutrino trapping does not occur even with a high mass accretion rate of $\dot{M} \sim 10 M_\odot$ s^{-1}. This indicates that the black hole spin plays a crucial role on the properties of accretion flows around a black hole.

They also find that the neutrino trapping occurs in the vicinity of the black hole ($r \lesssim 20 G M_{BH}/c^2$), as in our case. This indicates the importance of resolving the regions close to the black hole because the

seed of convection is formed there.

   Similar convective accretion flows as found in the present simulation were first predicted by Narayan and Yi [20] in studies of a self-similar solution of advection-dominated accretion flows (ADAFs), and were coined as convection-dominated accretion flows (CDAFs). While the CDAF-like accretion flows are formed in the outer region of the torus, flows in the inner region are similar to those of neutrino-domineted accretion flows (NDAFs) [21]. As found in the present simulation, the accretion flows in collapsar will be characterized by the inner NDAF-like and outer CDAF-like flows. As suggested by [22], the former may produce a GRB and the later may make a supernova explosions.

Acknowledgments

References

[1] T. Piran, T., Phys. Rep., 314, 575 (1999).

[2] S. E. Woosley and J. S. Bloom, Ann. Rev. Astron. Astrophys 44, 507 (2006).

[3] A. S. Fruchter et al., Nature 441, 463 (2006).

[4] M. Modjaz et al., Astron. J. 135, 1136 (2008).

[5] V. Bromm and A. Loeb, Astrophys. J. 642, 382 (2002).

[6] S.-C. Yoon and N. Langer, Astron. Astrophys. 443, 643 (2005); S.-C. Yoon, N. Langer, and C. Norman, Astron. Astrophys. 460, 199 (2006)

[7] S. E. Woosley and A. Heger, Astrophys. J. 637, 914 (2006).

[8] C. L. Fryer et al., Publ. Astron. Soc. Pacific, 119, 1211 (2007).

[9] R. G. Izzard, E. Ramirez-Ruiz, and C. A. Tout, Mon. Not. R. Astron. Soc. 348, 1215 (2004); P. Podsiadlowski et al., Astrophys. J. 607, L17 (2004)

[10] E. P. J. van den Heuvel and S.-C. Yoon, Astrophys. Space Sci. 311, 177 (2007); M. Cantiello et al., Astron. Astrophys. 465, L29 (2007).

[11] C. L. Fryer and A. Heger, Astrophys. J. 623, 302 (2005)

[12] T. K. Suzuki et al., Astrophys. J. 668, 435 (2007); E. Gaburov, J. C. Lombardi, and S. Portegies Zwart, Mon. Not. R. Astron. Soc. 383, L5 (2008)

[13] A. Heger et al., Astrophys. J. 591, 288 (2003).

[14] Y. Sekiguchi, Class. Quant. Grav. 27, 114107 (2010); Prog. Theor. Phys. 124, 331 (2010).

[15] H. Shen, H. Toki, K. Oyamatsu, and K. Sumiyoshi, Nucl. Phys. A, 637, 435 (1998).

[16] S. Rosswog and M. Liebendörfer, Mon. Not. R. Astron. Soc. 342, 673 (2003).

[17] K. Nakazato, K. Sumiyoshi and S. Yamada, Astrophys. J. 666, 1140 (2007).

[18] M. Shibata and S. L. Shapiro, Astrophys. J. Lett. 572, 39 (2002).

[19] W.-X. Chen and A. M. Beloborodov, Astrophys. J. 657, 383 (2007).

[20] R. Narayan and I. Yi, Astrophys. J. Lett. 428, 13 (1994).

[21] R. Popham, S. E. Woosley and C. Fryer, Astrophys. J. 518, 356 (1999).

[22] R. Narayan, T. Piran and P. Kumar, Astrophys. J. 557, 949 (2001).